RSC Advances

ROYAL SOCIETY OF CHEMISTRY

www.rsc.org/advances

Table of Contents Entry

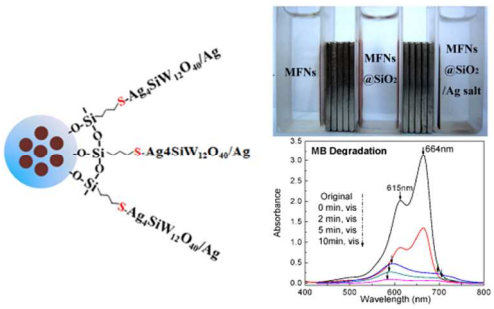

A novel superparamagnetic Ag@silver-based salt photocatalyst, MFNs@SiO_2@$Ag_4SiW_{12}O_{40}$/Ag, was created with highly efficient visible light photocatalytic performance and easy magnetic separation.

Synthesis of a Superparamagnetic MFNs@SiO_2@$Ag_4SiW_{12}O_{40}$/Ag Composite Photocatalyst, its Superior Photocatalytic Performance under Visible Light Illumination, and Easy Magnetic Separation

Wenshu Tang[a], Yu Su[a], Xiaoxin Wang[a], Qi Li[a,*], Shian Gao[a], and Jian Ku Shang[a,b]

[a]*Environment Functional Materials Division*

Shenyang National Laboratory for Materials Science

Institute of Metal Research, Chinese Academy of Sciences, Shenyang, 110016, P. R. China

[b]*Department of Materials Science and Engineering*

University of Illinois at Urbana-Champaign, Urbana, IL 61801, USA

*To whom correspondence should be addressed.

Address: 72 Wenhua Road

Shenyang, Liaoning Province, 110016, P. R. China

Phone: +86-24-83978028 (O), +86-24-23971215 (Fax)

E-mail: qili@imr.ac.cn

Abstract

A novel superparamagnetic Ag@silver-based salt photocatalyst, MFNs@SiO_2@$Ag_4SiW_{12}O_{40}$/Ag, was created, which demonstrated highly efficient photocatalytic performance under visible light illumination in both the degradation of methylene blue (MB) and the disinfection of *Escherichia coli* (*E. coli*) bacteria. In this composite photocatalyst, well-dispersed, superparamagnetic magnesium ferrite nanoparticle (MFNs) were used as the core for its easy magnetic separation capability. A passive SiO_2 mid-layer was used to separate MFNs and $Ag_4SiW_{12}O_{40}$, and form a strong bonding with silver ions for their loading after –SH surface modification. $Ag_4SiW_{12}O_{40}$ layer was subsequently formed by the reaction with silicotungstic acid to avoid the commonly adopted calcination procedure after deposition/precipitation, and silver nanoparticles were formed on the surface of $Ag_4SiW_{12}O_{40}$ layer after UV irradiation to further enhance their photocatalytic performance and stability under visible light illumination. The surface modification on the passive SiO_2 mid-layer and the bridging procedure for material loading developed in our approach could be readily applied to other material systems for the creation of novel composite materials with various functions.

Keywords: magnesium ferrite nanocrystallites, Ag salts, photocatalytic degradation, photocatalytic sterilization.

1. Introduction

Semiconductor-based photocatalysis could be a promising approach to solve energy and environmental problems faced by human beings now and in the near future if solar energy could be efficiently utilized[1]. Among various semiconductor-based photocatalysts, TiO_2 had been extensively studied during the last several decades because of its high chemical stability, good photoactivity, relatively low cost, and nontoxicity[2]. However, its photocatalytic capability is limited to only ultraviolet (UV) light (wavelength $\lambda < 400$ nm), which just occupies about 4% in the solar spectrum. To enhance their solar efficiency, extensive research efforts therefore had been made to explore photocatalysts that could be activated by visible light, including modified-TiO_2[3, 4], multimetal oxides[5-7], sulfides[8], oxynitrides[9], graphite oxide[10], C_3N_4[11], $BiVO_4$[12]and heterojunctions[13].

Recently, a series of silver-based compounds attracted much research attention due to their excellent performance as visible-light-driven photocatalysts, including AgX (X= Cl, Br, I)[14, 15], Ag_3PO_4[16], Ag_2CO_3[17], Ag_3VO_4[18], $AgSbO_3$[19], $AgNbO_3$[20], $AgIn(WO_4)_2$[21], $Ag_4SiW_{12}O_{40}$[22], silver titanates[23] and delafossite $AgMO_2$ (M = Al, Ga, In)[24]. With the enhancement by the localized surface plasmon resonance (LSPR) effect of silver nanoparticles in the visible light region, their photocatalytic performance and stability were further improved under visible light illumination[11, 21, 22]. For example, Huang et al. reported that plasmatic Ag@AgX (X= Cl, Br, I) exhibited highly efficient and stable photocatalytic activity under visible light illumination[14, 15], and Gondal et al. found that $Ag@Ag_3PO_4$ showed enhanced both UV and visible light photocatalytic activities in the degradation of Rhodamine B[25]. The photocatalytic performance of Ag@silver-based salt photocatalysts could also be tuned by altering the negative charged anions in this material system, and it had been reported that anions with higher charges led to a stronger photocatalytic

capability[22]. Thus, $Ag@Ag_4SiW_{12}O_{40}$ might be a promising candidate with a highly efficient visible-light-driven photocatalytic activity, and it should be further explored towards various technical applications, including the organic pollutant degradation, pathogen microorganism disinfection, and water splitting under visible-light illumination.

To remove nanomaterials from an aqueous environment efficiently and selectively after water treatment, magnetic separation was considered as a promising alternative, compared with the conventional centrifugation or filtration processes[26]. Magnetic photocatalysts of Ag@silver-based salt (ASS), such as $Fe_3O_4@SiO_2@AgCl$-Ag[27], AgCl doped $Fe_3O_4@SiO_2$[28], $Ag–AgI/Fe_3O_4@SiO_2$[29] and $Ag/AgBr/ Fe_3O_4@SiO_2$[30], had been reported. However, there were several drawbacks in these ASS synthesis processes. First, silver based compounds were immobilized on $Fe_3O_4@SiO_2$ cores with deposition/precipitation procedures, resulting in nonuniform morphology[27]. Second, the calcination procedure after deposition/precipitation increased energy consumption/cost and usually led to their aggregation and a subsequent lower surface-to-volume ratio, deteriorating their photocatalytic activity[27]. Third, incorporated magnetic cores may contain remanent magnetism and magnetic attraction existed between these nano-ASSs even without the external magnetic field for separation. So it was difficult to disperse them in water to have a better contact efficiency with pollutants[31]. Thus, new approaches should be developed to overcome these difficulties for the design and synthesis of novel magnetic ASSs with high photocatalytic performance.

We report here a novel superparamagnetic ASS, magnesium ferrite nanoparticles (MFNs)$@SiO_2@Ag_4SiW_{12}O_{40}$/Ag. In this photocatalyst material system, well-dispersed, superparamagnetic magnesium ferrite nanoparticles were used as the core[32-34]. A passive SiO_2 mid-layer was introduced to coat MFNs, which could separate MFNs and $Ag_4SiW_{12}O_{40}$ to

prevent the charge carrier recombination in MFNs for the enhancement of their photoactivity and provide an easy surface modification potential. After –SH modification on the SiO_2 mid-layer surface, silver ions could be uniformly bridged onto the surface of MFNs@SiO_2, and $Ag_4SiW_{12}O_{40}$ layer was subsequently formed by the reaction with silicotungstic acid to avoid the commonly adopted calcination procedure after deposition/precipitation. Finally, silver nanoparticles were formed on the surface of $Ag_4SiW_{12}O_{40}$ layer after UV irradiation to further enhance their photocatalytic performance and stability under visible light illumination, which was demonstrated in both the degradation of methylene blue (MB) and the disinfection of *Escherichia coli* (*E. coli*) bacteria.

2. Experimental Section

2.1. Chemicals and Material. Well-dispersed, superparamagnetic magnesium ferrite nanoparticles were synthesized as detailed in our previous report[33]. Tetraethyl orthosilicate (TEOS, $C_8H_{20}O_4Si$，99.9%, Tianjin Kermel Chemical Reagents Development Center, Tianjin, P. R. China), aqueous ammonia ($NH_3 \cdot H_2O$, 25~28%，Sinopharm Chemical Reagent Co., Ltd., Shanghai, P. R. China), mercaptopropyltriethoxy-silane (MPTES, $C_9H_{22}O_3SSi$，98%，Sinopharm Chemical Reagent Co., Ltd., Shanghai, P. R. China) and methylbenzene (C_7H_8，99.9%，Sinopharm Chemical Reagent Co., Ltd., Shanghai, P. R. China) were used to coat the SiO_2 layer on MFN to obtain MFN@SiO_2, and modify the SiO2 layer surface with –SH. Cetyl trimethyl ammonium bromide (CTAB, $C_{19}H_{42}BrN$，99 %，Sinopharm Chemical Reagent Co., Ltd., Shanghai, P. R. China), silver nitrate, sodium chloride, sodium carbonate, sodium phosphate and silicotungstic acid (99.9%，Sinopharm Chemical Reagent Co., Ltd., Shanghai, P. R. China) were used to synthesize MFNs@SiO_2/$Ag_4SiW_{12}O_{40}$ photocatalyst. Methylene blue ($C_{16}H_{18}ClN_3S_2$，

99 %，Shanghai Huyu biotechnology Co., Ltd, Shanghai, P. R. China) and *E.coli* bacteria (ATCC 15597, American type culture collection) were used for the photocatalytic degradation and disinfection experiments, respectively. Commercially available Degussa P25 TiO_2 nanoparticles (Evonik Industries, Germany) were used for comparison purpose.

2.2. Synthesis of MFNs@SiO_2/$Ag_4SiW_{12}O_{40}$ /Ag Photocatalyst. Figure 1 schematically shows the synthesis process of MFNs@SiO_2/$Ag_4SiW_{12}O_{40}$/Ag photocatalyst. 0.05 g superparamagnetic MFNs were firstly dispersed into a mixed solution of 80 mL ethanol and 20 mL deionized water, and ultrasonicated for 30 min. Then, 100 μL TEOS was added into the suspension dropwise under mechanical stirring at 200 r/min, and 2 mL $NH_3 \cdot H_2O$ was added into it quickly after 5 min. The suspension was kept stirring for 6 h before MFN@SiO_2 nanoparticles were magnetically separated and re-dispersed into 5 mL ethanol. These steps were repeated to get enough amounts of MFN@SiO_2 nanoparticles dispersed in ethanol. 50 mL of such suspension was transferred into a 250 mL three-neck flask and kept at 80 ^oC in a water bath. 200 μL MPTES was then added dropwise into the flask and the suspension was refluxed for 12 h. After magnetic separation and washing with deionized water and ethanol for three times, MFNs@SiO_2 with –SH surface modification were obtained.

These MFNs@SiO_2 with –SH surface modification were then dispersed into 50 mL silver nitrate solution (0.01 M) by ultrasonication, and the Ag^+ adsorption lasted for 12 h. Nanoparticle samples were magnetically separated and washed with deionized water until no Ag^+ was found in water. Then, they were re-dispersed in 50 mL deionized water with a proper amount of CTAB, and 50 mL silicotungstic acid solution (0.0025 M) was slowly added into the suspension to react with Ag^+ bridged on the surface of MFNs@SiO_2 to form $Ag_4SiW_{12}O_{40}$. After being magnetically separated and dried at 80 ^oC in a vacuum oven for 8 h, MFNs@SiO_2/$Ag_4SiW_{12}O_{40}$ samples were

obtained. Finally, MFNs@SiO_2/$Ag_4SiW_{12}O_{40}$ samples were irradiated for 0.5 h, 1 h, 2 h, 4 h and 8 h, respectively, by UV light (365±15 nm, 5 mW/cm^2) to form Ag nanoparticles on the surface of $Ag_4SiW_{12}O_{40}$ layer.

2.3. Materials Characterization. The crystal structures of samples were analyzed by D/MAX-2004-X-ray powder diffractometer (Rigaku Corporation, Tokyo, Japan) with Ni-filtered Cu (0.15418 nm) radiation at 56 kV and 182 mA. Their morphologies were examined by transmission electron microscopy (TEM) and field emission scanning electron microscopy (FESEM). TEM observations were carried out on a JEM 2100 transmission electron microscope (JEOL Corporation, Tokyo, Japan) operated at 200 kV. TEM samples were made by dispersing a thin film of samples on Cu grid pre-coated with thin and flat carbon film. SEM images were obtained with a SUPRA35 Field Emission Scanning Electron Microscope (ZEISS, Germany). SEM samples were prepared by applying a drop of the sample on a conductive carbon tape, and drying in air. Prior to imaging, the sample was sputtered with gold for 20 s (Emitech K575 Sputter Coater, Emitech Ltd., Ashford Kent, UK). BET surface area was measured by N_2 adsorption-desorption isotherm with an Autosorb-1 Series Surface Area and Pore Size Analyzers (Quantachrome Instruments, Boynton Beach, FL, U.S.A.). The surface chemical states of the samples were examined by X–ray photoelectron spectroscopy (XPS) using an ESCALAB250 X–ray Photoelectron Spectrometer (Thermo Fisher Scientific Inc., Waltham, MA, U.S.A.) with an Al K anode (1486.6 eV photon energy, 0.05 eV photon energy resolution, 300 W). FTIR spectroscope (Bruker TENSOR 27, MCT detector) was used to investigate the surface organic functional groups. Samples for FTIR observation were ground with spectral grade KBr in an agate mortar. Then a fixed amount of sample (1%w:w) in KBr was used to prepare all the pellets. The UV-vis spectra of samples were measured on a UV-Vis 2550 spectrophotometer (Shimadzu

Corporation, Kyoto, Japan). To explore the influence of SiO_2 coating and Ag salt loading on the magnetic properties of samples, MPMS-XL Superconducting Quantum Interference Device Magnetometer (Quantum Design, U.S.A.) was used to measure the magnetization curve with external magnetic field of 0 ~ 1 T.

2.4. Photocatalytic Degradation of Methylene Blue under Visible Light Illumination. Methylene blue (MB) was used as a model organic pollutant to evaluate the photocatalytic activity of samples under visible light illumination. The initial MB concentration was 1×10^{-5} M, and a fixed concentration of 0.5 mg photocatalyst/mL solution was used in the photocatalytic degradation experiments. Photocatalysts were firstly dispersed in MB solutions by mechanical stirring for 30 min in dark to reach adsorption equilibrium before visible light illumination started. A 300 W xenon lamp (PLS-SXE300, Beijing Perfect Light Technology Co., Ltd., Beijing, P. R. China) was used as the light source, which has a glass filter to provide zero light intensity below 400 nm. The light intensity striking the MB solution was at ca. 23 mW/cm^2, as measured by a FZ-A optical Radiometer (Photoelectric Instrument Factory of Beijing Norman University, Beijing, P. R. China). At each time interval, photocatalysts were magnetically separated, and the light absorption of the clear solution at ~ 663.5 nm was measured by the UV-2550 spectrophotometer to determine the MB remaining concentration. P25 TiO_2 nanoparticles were also used in the photocatalytic degradation of MB experiments for comparison purpose under the same experimental conditions. All analyses were in triplicate.

2.5. Photocatalytic Disinfection of Bacteria Escherichia coli (E. coli) under Visible Light Illumination. Wild-type *E. coli* AN 387 (ATCC 15597, the American Type Culture Collection, Manasss, VA, USA) was used for photocatalytic disinfection experiment under visible light illumination, which is a commonly used non-pathogenic bacterium with a short reproductive

cycle. After overnight culture, *E. coli* cells were diluted to a cell suspension (ca. 10^7 cfu/mL) in buffer solution (0.05 M KH_2PO_4 and 0.05 M K_2HPO_4, pH 7.0) prior to the use for photocatalytic disinfection experiments, and the fixed concentration of 1 mg photocatalyst/mL cell suspension was used for Degussa P25 TiO_2 nanoparticles, and 0.05 mg photocatalyst/mL cell suspension was used for MFNs@SiO_2/$Ag_4SiW_{12}O_{40}$/Ag photocatalysts. All solid or liquid materials had been autoclaved for 30 min at 121 ^oC before use. The same visible light source was used as in the photocatalytic degradation of MB. In the photocatalytic disinfection experiment, aliquot of 10 mL *E. coli* cell suspension was pipetted onto a sterile 50X10 mm petri dish with photocatalytic powder samples placed at the bottom. At regular time intervals, 100 μL of aliquots of the powder-treated cell suspensions were withdrawn in sequence. After appropriate dilutions in buffer solution, aliquot of 100 μL was spread onto an agar medium plate and incubated at 37 ^oC for 48 h, and the number of viable cells in terms of colony-forming units was counted. The survival ratio of *E. coli* was determined by the ratio of N_t/N_0, where N_0 and N_t are the numbers of colony-forming units at the initial and each following time interval, respectively. Tests were also performed in the dark in the presence of the photocatalyst for comparison. Analyses were in triplicate, and control runs were carried out each time under the same experiment conditions, but without any photocatalytic materials.

3. Results and Discussion

3.1. Creation of MFNs@SiO_2/$Ag_4SiW_{12}O_{40}$/Ag Photocatalyst. Figure 2a shows the TEM image of MFNs, in which well-dispersed nanocrystallites were observed and their size was around several nanometers. After the coating with SiO_2 by the Stöber reaction[35], well-dispersed MFNs@SiO_2 core/shell structured nanoparticles were created, in which SiO_2 shell wrapped a

bunch of MFNs as the superparamagnetic core to provide strong magnetic attraction for their effective magnetic separation as demonstrated clearly in the insert image of their TEM observation in Figure 2b. The particle size distribution of these MFNs@SiO_2 nanoparticles was relatively small at ~ 100 to 200 nm, and their surface was relatively smooth. The MFNs/TEOS ratio was carefully modulated to obtain samples with good dispersity, small size, and enough MFNs as the superparamagnetic core for proper magnetic separation.

To enhance the dispersion and subsequent contact efficiency with pollutants in water, a non-traditional, three-step process was adopted for the deposition of $Ag_4SiW_{12}O_{40}$ layer onto the surface of MFNs@SiO_2 nanoparticles. In the first step, the surface of MFNs@SiO_2 nanoparticles was modified to have –SH by the reaction with MPTES. According to Pearson's HSAB principle[36], –SH is a typical soft alkaline coordination group which has a strong attraction with soft acidic coordination groups like Ag^+. Thus, Ag^+ could be strongly adsorbed onto the surface of MFNs@SiO_2 nanoparticles in the second step because of its interaction with -SH. In the third step, the active $Ag_4SiW_{12}O_{40}$ layer was formed on the surface of MFNs@SiO_2 nanoparticles by the following reaction with silicotungstic acid. This process eliminated the calcination procedure commonly adopted in the deposition of silver salts onto substrates, and could form silver salt layers strongly attached to substrates. The $Ag_4SiW_{12}O_{40}$ loading amount could be estimated by the sample weight change before Ag^+ adsorption and after the reaction with silicotungstic acid, and a relatively large loading amount of ~ 24 wt% was achieved in this process. Figure 2c shows the SEM image of MFNs@SiO_2/$Ag_4SiW_{12}O_{40}$ nanoparticles, which demonstrated that a rough layer was formed on the smooth surface of MFNs@SiO_2 nanoparticles. The insert image in Figure 2c shows the high magnification SEM image of a MFNs@SiO_2/$Ag_4SiW_{12}O_{40}$ nanoparticle, which clearly demonstrated that this rough layer was composed of fine

nanoparticles with size ~10 to 20 nm. A rough layer of $Ag_4SiW_{12}O_{40}$ could increase their contact area with pollutants in water, beneficial to their photocatalytic performance.

Figure 2d compares the FTIR spectra of samples synthesized during this process, which confirms the formation of MFNs@SiO_2/$Ag_4SiW_{12}O_{40}$ nanoparticles. The FTIR spectrum of MFNs was demonstrated by curve a, in which their two characteristic absorption bands at ~ 593 cm^{-1} and 442 cm^{-1} could be observed, corresponding to the vibration of tetrahedral and octahedral sites, respectively[34]. After SiO_2 coating, a characteristic Si-O bond peak (980~1220 cm^{-1})[37] occurred in the FTIR spectrum of MFNs@SiO_2 nanoparticles (curve b in Figure 2d), while the intensity of the two characteristic peaks of MFNs (~ 593 and 442 cm^{-1}) was largely depressed. These changes suggested clearly that SiO_2 coating was formed on MFNs, which was in accordance with the TEM observation (Figure 2b). After the reaction with MPTES, the characteristic –SH peak (~ 2547 cm^{-1}) could be observed in curve c, indicating the successful surface –SH modification. Curve d shows the FTIR spectrum of MFNs@SiO_2/$Ag_4SiW_{12}O_{40}$ nanoparticles. After Ag^+ adsorption and the reaction with silicotungstic acid to form $Ag_4SiW_{12}O_{40}$ layer, the –SH peak disappeared, while the vibration absorption peak of W-O bond and W-O-W bond appeared at 978.2 cm^{-1} and 794.4 cm^{-1}, respectively, demonstrating that –SH on the surface of MFN@SiO_2 nanoparticles played the key role in the bridging of $Ag_4SiW_{12}O_{40}$ onto the surface of MFN@SiO_2 nanoparticle.

Finally, UV light illumination was used to form Ag nanoparticles on the surface of $Ag_4SiW_{12}O_{40}$ layer to further enhance its photocatalytic performance and stability. Figure 2e shows the XRD patterns of MFNs@SiO_2/$Ag_4SiW_{12}O_{40}$ nanoparticles after UV illuminations for different times. Without UV illumination, only the diffraction peaks of $Ag_4SiW_{12}O_{40}$ could be observed, which further illustrated that the SiO_2 layer could effectively wrap MFNs to avoid their

contact with the $Ag_4SiW_{12}O_{40}$ layer. After UV illumination, Ag nanoparticles were formed due to the photo-decomposition of silver salts. Diffraction peaks of Ag (111) ($2\theta \sim 38.08^o$), Ag (220) ($2\theta \sim 64.48^o$) and Ag (311) ($2\theta \sim 77.36^o$) could be observed on samples after 2 h and more UV illumination treatment, which clearly demonstrated the formation of Ag nanoparticles. With the increase of UV illumination time, their peak intensities increased gradually, indicating the increase of Ag nanoparticles formed. Figure 2f shows the high resolution XPS scans over Ag 3d peaks of MFNs@SiO_2/$Ag_4SiW_{12}O_{40}$ nanoparticles after UV illuminations for different times. Without UV illumination, the Ag 3d 5/2 peak was at ~ 368.5 eV and the Ag 3d 3/2 peak was at ~ 374.5 eV, indicating that silver was at its oxidized state as Ag^+. With the increase of UV illumination time, the Ag 3d peaks got broader and the peak positions gradually moved to the lower end, also indicating the formation of metallic silver (3d 5/2 peak ~ 368.0 eV) from light reduction on these samples[38].

3.2. The Magnetic Properties of MFNs@SiO_2/$Ag_4SiW_{12}O_{40}$/Ag Photocatalyst. The magnetic properties of MFNs@SiO_2/$Ag_4SiW_{12}O_{40}$/Ag photocatalyst are critical to its separation performance after water treatment. Figure 3a compares the magnetic field-dependent behaviors of MFNs, MFNs@SiO_2 nanoparticles, and MFNs@SiO_2/$Ag_4SiW_{12}O_{40}$/Ag nanoparticles at room temperature. All three samples demonstrated the typical superparamagnetic behavior with zero remanence and zero coercivity, which was not affected by SiO_2 coating or the further coating of $Ag_4SiW_{12}O_{40}$/Ag layer. The saturation magnetization, M_s, could be obtained by extrapolating a graph of M vs. 1/H to $1/H \rightarrow 0$ (for H > 10 kOe). At room temperature, MFNs possessed a high M_s of ~ 27.4 emu/g. The M_s of MFNs@SiO_2 nanoparticles dropped to ~ 16.3 emu/g due to the inclusion of nonmagnetic SiO_2 coating, while the M_s of MFNs@SiO_2/$Ag_4SiW_{12}O_{40}$/Ag nanoparticles did not decrease much after the further loading of photocatalytic $Ag_4SiW_{12}O_{40}$/Ag

layer. Figure 3b shows that all three samples could disperse well in DI water when there was no external magnetic field, which could be attributed to their supermagnetic behavior. So, no magnetic attraction existed when there was no external magnetic field applied during the water treatment, beneficial to their better dispersion and the subsequent better contact efficiency with pollutants in water. When an external magnetic field was applied for just 5 min, all three samples were efficiently separated from water as shown in Figure 3b. This observation demonstrated that although the M_s of MFNs@SiO_2/$Ag_4SiW_{12}O_{40}$/Ag nanoparticles was lower than that of MFNs, it was strong enough for the efficient separation of these photocatalysts from water, which is very desirable for its easy recovery after water treatment and enhances its application potential in real practice.

3.3. Optical Properties of MFNs@SiO_2/$Ag_4SiW_{12}O_{40}$/Ag Photocatalyst. The optical properties of MFNs@SiO_2/$Ag_4SiW_{12}O_{40}$/Ag photocatalysts with different UV treatment time were investigated by measuring their diffuse reflectance spectrum. From the reflectance data, optical absorbance can be approximated by the Kubelka-Munk function, as given by Eq. (1):

$$F(R) = \frac{(1-R)^2}{2R} \qquad (1)$$

where R is the diffuse reflectance[39]. Figure 4 shows their light absorbance spectra (in term of Kubelka-Munk equivalent absorbance units). Without UV treatment, $Ag_4SiW_{12}O_{40}$ demonstrated an evident light absorption into the visible light region, and its absorbance stopping edge was found at ~ 460 nm. After UV treatment, all $Ag_4SiW_{12}O_{40}$/Ag samples demonstrated enhanced visible light absorption than $Ag_4SiW_{12}O_{40}$. With the increase of the UV treatment time, their visible light absorption gradually increased until the UV treatment time reached 4 h. Further UV treatment did not show more enhancement effect. A broad absorption peak could be observed for all $Ag_4SiW_{12}O_{40}$/Ag samples from ~ 500 nm to 600 nm, which should correspond to the

absorption by Ag nanoparticles from LSPR effect.

3.4. Photocatalytic Degradation of Methylene Blue by MFNs@SiO_2/$Ag_4SiW_{12}O_{40}$/Ag Photocatalyst under Visible Light Illumination. The photocatalytic activities of MFNs@SiO_2/$Ag_4SiW_{12}O_{40}$/Ag photocatalysts were first demonstrated by their degradation effect on a model organic contaminant, methylene blue (MB), under visible light illumination. Prior to the visible light illumination, photocatalysts were dispersed in MB solutions by mechanical stirring for 30 min in dark to reach adsorption equilibrium. Figure 5a shows the representative light absorption spectra of MB solutions at different treatment times by the MFNs@SiO_2/$Ag_4SiW_{12}O_{40}$/Ag photocatalyst with 4 h prior UV irradiation. During the dark adsorption, large portion of MB was removed as demonstrated by the decrease of light absorption for MB solution from the "original" curve to the "0 min" curve. After the visible light illumination began, the light absorption of MB solution decreased steadily, indicating the continuous decrease of MB concentration. After just 10 min, the light absorption of MB solutions dropped to near zero, indicating a near complete degradation of MB. A clear change was observed on the shape of MB light absorption curve as new peaks occurred besides the characteristic MB peaks at 664 nm and 615 nm after the visible light illumination began. The insert image in Figure 5a shows MB solutions at different treatment times. After visible light illumination began, the MB solution color changed from pure blue to light purple, which was in accordance with their light adsorption spectra. This observation suggested that intermediate products were produced during the photocatalytic degradation process[40].

Figure 5b shows the relative residue MB concentration after being treated by MFNs@SiO_2/$Ag_4SiW_{12}O_{40}$/Ag photocatalysts with different prior UV irradiation time under visible light illumination, compared with that treated by P25 TiO_2 nanoparticles under the same

visible light illumination. MFNs@SiO_2/$Ag_4SiW_{12}O_{40}$/Ag photocatalysts demonstrated a better adsorption and a much faster degradation on MB than P25 TiO_2 nanoparticles. With only 10 minute visible light illumination, the relative MB concentration dropped to around zero by MFNs@SiO_2/$Ag_4SiW_{12}O_{40}$/Ag photocatalysts, while the relative MB concentration treated by P25 TiO_2 nanoparticles was still round 90% and most of the drop was due to its adsorption onto P25 TiO_2 nanoparticles. The prior UV irradiation treatment affected their photocatalytic degradation effect on MB. With the increase of the UV irradiation time from zero up to 4 h, the photocatalytic degradation efficiency of MFNs@SiO_2/$Ag_4SiW_{12}O_{40}$/Ag photocatalysts increased, while the further increase of UV irradiation time to 8h demonstrated a deteriorated effect on their photocatalytic degradation efficiency. The slope of the MB degradation curve in Figure 5b represents the MB degradation rate at certain treatment time. The initial MB degradation rate was ~ 0.0038 mg/(g·min) when Degussa P25 TiO_2 nanoparticles were used. The initial MB degradation rate by MFNs@SiO_2/$Ag_4SiW_{12}O_{40}$ photocatalyst without prior UV irradiation increased to ~ 0.115 mg/(g·min), ~ 30 times as that of Degussa P25 TiO_2 nanoparticles. The initial MB degradation rate by the MFNs@SiO_2/$Ag_4SiW_{12}O_{40}$/Ag photocatalyst with 4 h prior UV irradiation further increased to ~ 0.144 mg/(g·min), ~ 38 times as that of Degussa P25 TiO_2 nanoparticles and ~ 1.27 times as that of the MFNs@SiO_2/$Ag_4SiW_{12}O_{40}$ photocatalyst without prior UV irradiation. Thus, these MFNs@SiO_2/$Ag_4SiW_{12}O_{40}$ photocatalysts demonstrated superior photocatalytic performance under visible light illumination.

3.5. Photocatalytic disinfection of Escherichia coli Bacteria by MFNs@SiO_2/$Ag_4SiW_{12}O_{40}$/Ag Photocatalyst under Visible Light Illumination. The superior photocatalytic performance of these MFNs@SiO_2/$Ag_4SiW_{12}O_{40}$/Ag photocatalysts under visible light illumination was further demonstrated by their photocatalytic disinfection effect on the

viability of *E. coli* cells. Figure 6a shows the survival ratio of *E. coli* with the treatments by the MFNs@SiO_2/$Ag_4SiW_{12}O_{40}$/Ag photocatalyst with 4 h prior UV irradiation under visible light illumination and in dark, respectively, compared with that by Degussa P25 TiO_2 nanoparticles under visible light illumination. When there was no photocatalyst presence, no obvious *E. coli* disinfection was observed under visible light illumination (not shown in Figure 6a). Degussa P25 TiO_2 nanoparticles demonstrated a weak disinfection capability on *E. coli* bacteria. After 10 min treatment, the survival ratio of *E. coli* bacteria was still ~ 40%, which could be attributed to its weak photocatalytic activity under visible light illumination from its mixture nature of both anatase and rutile phases. When the MFNs@SiO_2/$Ag_4SiW_{12}O_{40}$/Ag photocatalyst was present, it demonstrated a moderate disinfection effect on *E. coli* without light illumination. After 10 min treatment, the survival ratio of *E. coli* dropped to ~ 3 %, which should come from the well-known bactericidal effect of silver. Under visible light illumination, however, the MFNs@SiO_2/$Ag_4SiW_{12}O_{40}$/Ag photocatalyst demonstrated a much better disinfection effect on *E. coli*. The survival ratio of *E. coli* continuously decreased with the increase of the treatment time. After just 10 min treatment, the survival ratio of *E. coli* dropped to ~ $3x10^{-6}$, which was more than 5 magnitudes lower than that treated by Degussa P25 TiO_2 nanoparticles, although its usage was just 5% as that of Degussa P25 TiO_2 nanoparticles. The *E. coli* survival ratio treated by the MFNs@SiO_2/$Ag_4SiW_{12}O_{40}$/Ag photocatalyst under visible light illumination was about 4 magnitudes lower than that without visible light illumination. From this comparison, it is clear that its demonstrated superior bactericidal effect on *E. coli* under visible light illumination could be mainly attributed to the superior photocatalytic performance of these MFNs@SiO_2/$Ag_4SiW_{12}O_{40}$/Ag photocatalysts, not the modest bactericidal effect from silver itself.

Figure 6b and 6c show the SEM images of *E. coli* cells before and after photocatalytic treatment by the MFNs@SiO_2/$Ag_4SiW_{12}O_{40}$/Ag photocatalyst under visible light illumination. Before the photocatalytic treatment, *E. coli* cells had damage-free surface. During the photocatalytic disinfection treatment, *E. coli* cells could not sustain their structure. Severe surface damages were clearly observed on these cells. Large holes and pits occurred on their cell membranes, and they lost their flagella completely. This observation indicated that the disinfection of *E. coli* cells by the MFNs@SiO_2/$Ag_4SiW_{12}O_{40}$/Ag photocatalyst was irreversible due to its destructive nature. The MFNs@SiO_2/$Ag_4SiW_{12}O_{40}$/Ag photocatalyst also demonstrated a good stability during the photocatalytic disinfection of *E. coli* cells for four consecutive runs. After each run, the MFNs@SiO_2/$Ag_4SiW_{12}O_{40}$/Ag photocatalyst was separated from the *E. coli* cell suspension by an external magnetic field, washed with DI water, and then reused for the next run. As demonstrated in Figure 6d, the survival ratio of *E. coli* all dropped to ~ 10^{-6} after just 10 min treatment for all four runs. The demonstrated good stability was beneficial for their potential applications.

3.6. Photocatalytic Mechanism of MFNs@SiO_2/$Ag_4SiW_{12}O_{40}$/Ag Photocatalyst. Figure 7 schematically illustrates the mechanism for the superior photocatalytic performance of MFNs@SiO_2/$Ag_4SiW_{12}O_{40}$/Ag photocatalyst under visible light illumination. Only $Ag_4SiW_{12}O_{40}$ shell and Ag nanoparticles were demonstrated in this illustration to make it easier for understanding. After being treated with UV irradiation, Ag nanoparticles were formed due to the photo-decomposition of $Ag_4SiW_{12}O_{40}$[22]. Thus, the localized surface plasmon resonance (LSPR) effect from Ag nanoparticles on the surface of $Ag_4SiW_{12}O_{40}$ could enhance its light absorption in the visible light region[22]. Ag nanoparticles could promote the electron/hole separation in $Ag_4SiW_{12}O_{40}$ when it was under visible light illumination by acting as the electron trapping

center, which further enhance its photocatalytic performance. The electron trapping on Ag nanoparticles could reduce and finally inhibit the further photo-decomposition of $Ag_4SiW_{12}O_{40}$. Thus, the prior UV treatment of the MFNs@SiO_2/$Ag_4SiW_{12}O_{40}$ photocatalyst could also enhance its stability.

4. Conclusions

In summary, MFNs@SiO_2/$Ag_4SiW_{12}O_{40}$/Ag photocatalyst was synthesized by our approach, which overcame the difficulties in the current synthesis practices of magnetic ASSs and created a novel magnetic ASS photocatalyst with highly efficient photocatalytic performance under visible light illumination and easy magnetic separation capability. The initial MB degradation rate by MFNs@SiO_2/$Ag_4SiW_{12}O_{40}$/Ag photocatalyst with 4 h prior UV irradiation was ~ 38 times as that of Degussa P25 TiO_2 nanoparticles, and the survival ratio of *E. coli* treated by it was more than 5 magnitudes lower than that treated by Degussa P25 TiO_2 nanoparticles even though its usage was just 5% as that of Degussa P25 TiO_2 nanoparticles. Furthermore, the surface modification on the passive SiO_2 mid-layer and the bridging procedure for material loading developed in our approach could be readily applied to other material systems for the creation of novel composite materials with various functions.

Acknowledgments

The experimental assistance on *E. coli* culture by Ms. Mian Song and Ms. Shuang Jiao was greatly appreciated. This study was supported by the National Natural Science Foundation of China (Grant No. 51102246), the Knowledge Innovation Program of Institute of Metal Research, Chinese Academy of Sciences (Grant No. Y0N5A111A1), the Youth Innovation Promotion

406 Association, Chinese Academy of Sciences (Grant No. Y2N5711171), and the Scientific Research
407 Foundation for the Returned Overseas Chinese Scholars, State Education Ministry, P. R. China.
408

References

1. M. R. Hoffmann, S. T. Martin, W. Y. Choi and D. W. Bahnemann, *Chemical Reviews*, 1995, 95, 69-96.
2. K. Hashimoto, H. Irie and A. Fujishima, *Japanese Journal of Applied Physics Part 1-Regular Papers Brief Communications & Review Papers*, 2005, 44, 8269-8285.
3. Q. Li, Y. W. Li, P. G. Wu, R. C. Xie and J. K. Shang, *Advanced Materials*, 2008, 20, 3717-3723.
4. R. Asahi, T. Morikawa, T. Ohwaki, K. Aoki and Y. Taga, *Science*, 2001, 293, 269-271.
5. D. F. Wang, T. Kako and J. H. Ye, *Journal of the American Chemical Society*, 2008, 130, 2724-2725.
6. Z. G. Zou, J. H. Ye, K. Sayama and H. Arakawa, *Nature*, 2001, 414, 625-627.
7. J. W. Tang, Z. G. Zou and J. H. Ye, *Angewandte Chemie-International Edition*, 2004, 43, 4463-4466.
8. N. Z. Bao, L. M. Shen, T. Takata and K. Domen, *Chemistry of Materials*, 2008, 20, 110-117.
9. K. Maeda, K. Teramura, D. L. Lu, T. Takata, N. Saito, Y. Inoue and K. Domen, *Nature*, 2006, 440, 295-295.
10. T. F. Yeh, J. M. Syu, C. Cheng, T. H. Chang and H. S. Teng, *Advanced Functional Materials*, 2010, 20, 2255-2262.
11. X. C. Wang, K. Maeda, A. Thomas, K. Takanabe, G. Xin, J. M. Carlsson, K. Domen and M. Antonietti, *Nature Materials*, 2009, 8, 76-80.
12. A. Kudo, K. Ueda, H. Kato and I. Mikami, *Catalysis Letters*, 1998, 53, 229-230.
13. X. Zong, H. J. Yan, G. P. Wu, G. J. Ma, F. Y. Wen, L. Wang and C. Li, *Journal of the American Chemical Society*, 2008, 130, 7176-7177.
14. P. Wang, B. B. Huang, X. Y. Qin, X. Y. Zhang, Y. Dai, J. Y. Wei and M. H. Whangbo, *Angewandte Chemie-International Edition*, 2008, 47, 7931-7933.
15. P. Wang, B. B. Huang, X. Y. Zhang, X. Y. Qin, H. Jin, Y. Dai, Z. Y. Wang, J. Y. Wei, J. Zhan, S. Y. Wang, J. P. Wang and M. H. Whangbo, *Chemistry-a European Journal*, 2009, 15, 1821-1824.
16. Z. G. Yi, J. H. Ye, N. Kikugawa, T. Kako, S. X. Ouyang, H. Stuart-Williams, H. Yang, J. Y. Cao, W. J. Luo, Z. S. Li, Y. Liu and R. L. Withers, *Nature Materials*, 2010, 9, 559-564.
17. H. J. Dong, G. Chen, J. X. Sun, C. M. Li, Y. G. Yu and D. H. Chen, *Applied Catalysis B-Environmental*, 2013, 134, 46-54.
18. X. X. Hu and C. Hu, *Journal of Solid State Chemistry*, 2007, 180, 725-732.
19. T. Kako, N. Kikugawa and J. Ye, *Catalysis Today*, 2008, 131, 197-202.
20. G. Q. Li, S. C. Yan, Z. Q. Wang, X. Y. Wang, Z. S. Li, J. H. Ye and Z. G. Zou, *Dalton Transactions*, 2009, DOI: Doi 10.1039/B906799j, 8519-8524.
21. B. Hu, L. H. Wu, S. J. Liu, H. B. Yao, H. Y. Shi, G. P. Li and S. H. Yu, *Chemical Communications*, 2010, 46, 2277-2279.
22. H. Huang, X. R. Li, Z. H. Kang, Y. Liu, H. T. Li, X. D. He, S. Y. Lian, J. L. Liu and S. T. Lee, *Dalton Transactions*, 2010, 39, 10593-10597.
23. Q. Y. Li, T. Kako and J. H. Ye, *Applied Catalysis a-General*, 2010, 375, 85-91.
24. H. Dong, Z. H. Li, X. M. Xu, Z. X. Ding, L. Wu, X. X. Wang and X. Z. Fu, *Applied Catalysis B-Environmental*, 2009, 89, 551-556.
25. M. A. Gondal, X. F. Chang, W. E. I. Sha, Z. H. Yamani and Q. Zhou, *J Colloid Interf Sci*, 2013, 392, 325-330.
26. W. Z. Sun, Q. Li, S. Gao and J. K. Shang, *Journal of Materials Chemistry A*, 2013, 1, 9215-9224.
27. C. H. An, X. J. Ming, J. Z. Wang and S. T. Wang, *Journal of Materials Chemistry*, 2012, 22, 5171-5176.

28. N. Mahmed, O. Heczko and S. P. Hannula, *Adaptive, Active and Multifunctional Smart Materials Systems*, 2013, 77, 184-189.
29. J. F. Guo, B. W. Ma, A. Y. Yin, K. N. Fan and W. L. Dai, *Applied Catalysis B-Environmental*, 2011, 101, 580-586.
30. G. T. Li, K. H. Wong, X. W. Zhang, C. Hu, J. C. Yu, R. C. Y. Chan and P. K. Wong, *Chemosphere*, 2009, 76, 1185-1191.
31. X. X. Yu, S. W. Liu and J. G. Yu, *Applied Catalysis B-Environmental*, 2011, 104, 12-20.
32. W. S. Tang, Y. Su, Q. Li, S. Gao and J. K. Shang, *Journal of Materials Chemistry A*, 2013, 1, 830-836.
33. W. S. Tang, Y. Su, Q. Li, S. A. Gao and J. K. Shang, *Rsc Advances*, 2013, 3, 13961-13967.
34. W. S. Tang, Y. Su, Q. Li, S. A. Gao and J. K. Shang, *Water Research*, 2013, 47, 3624-3634.
35. W. Stober, A. Fink and E. Bohn, *J Colloid Interf Sci*, 1968, 26, 62-69.
36. R. G. Pearson, *Inorganica Chimica Acta*, 1995, 240, 93-98.
37. K. El-Boubbou, C. Gruden and X. Huang, *Journal of the American Chemical Society*, 2007, 129, 13392-13393.
38. K. T. V. Rao, P. S. S. Prasad and N. Lingaiah, *Green Chemistry*, 2012, 14, 1507-1514.
39. J. Tauc, Grigorov.R and A. Vancu, *Physica Status Solidi*, 1966, 15, 627-637.
40. G. Y. Zhang, Y. Q. Sun, D. Z. Gao and Y. Y. Xu, *Materials Research Bulletin*, 2010, 45, 755-760.

Figure Captions:

Figure 1. The schematic illustration of the synthesis process of MFNs@SiO_2/$Ag_4SiW_{12}O_{40}$/Ag photocatalyst (A: MFNs, B: MFNs@SiO_2, C: MFNs@SiO_2 with –SH surface modification, D: MFNs@SiO_2/Ag^+, E: MFNs@SiO_2/$Ag_4SiW_{12}O_{40}$, and F: MFNs@SiO_2/$Ag_4SiW_{12}O_{40}$/Ag).

Figure 2. (a) The TEM image of MFNs. (b) The TEM image of MFNs@SiO_2 core/shell structured nanoparticles. (c) SEM image of MFNs@SiO_2/$Ag_4SiW_{12}O_{40}$ nanoparticles. (d) The FTIR spectra of MFNs, MFNs@SiO_2, MFNs@SiO_2-SH, and MFNs@SiO_2/$Ag_4SiW_{12}O_{40}$ samples. (e) The XRD patterns of MFNs@SiO_2/$Ag_4SiW_{12}O_{40}$ nanoparticles after UV illuminations for different times. (f) The high resolution XPS scans over Ag 3d peaks of MFNs@SiO_2/$Ag_4SiW_{12}O_{40}$ nanoparticles after UV illuminations for different times.

Figure 3. (a) The magnetic field-dependent behaviors of MFNs, MFNs@SiO_2, and MFNs@SiO_2/$Ag_4SiW_{12}O_{40}$/Ag at room temperature. (b) Magnetic separation of MFNs, MFNs@SiO_2, and MFNs@SiO_2/$Ag_4SiW_{12}O_{40}$/Ag from water under external magnetic field for 5 min.

Figure 4. The light absorbance of MFNs@SiO_2/$Ag_4SiW_{12}O_{40}$/Ag photocatalysts with different UV treatment time.

Figure 5. (a) The representative light absorption spectra of MB solutions at different treatment times by the MFNs@SiO_2/$Ag_4SiW_{12}O_{40}$/Ag photocatalyst with 4 h prior UV irradiation. (b) The relative residue MB concentration after being treated by MFNs@SiO_2/$Ag_4SiW_{12}O_{40}$/Ag

photocatalysts with different prior UV irradiation time under visible light illumination, compared with that treated by P25 TiO_2 nanoparticles under the same visible light illumination.

Figure 6. (a) The survival ratio of *E. coli* with the treatments by the MFNs@SiO_2/$Ag_4SiW_{12}O_{40}$/Ag photocatalyst with 4 h prior UV irradiation under visible light illumination and in dark, respectively, compared with that by Degussa P25 TiO_2 nanoparticles under visible light illumination. The SEM images of *E. coli* cells (b) before and (c) after photocatalytic treatment by the MFNs@SiO_2/$Ag_4SiW_{12}O_{40}$/Ag photocatalyst under visible light illumination. (d) The survival ratio of *E. coli* for four consecutive runs.

Figure 7. The schematic illustration of the mechanism for the superior photocatalytic performance of MFNs@SiO_2/$Ag_4SiW_{12}O_{40}$/Ag photocatalyst under visible light illumination.

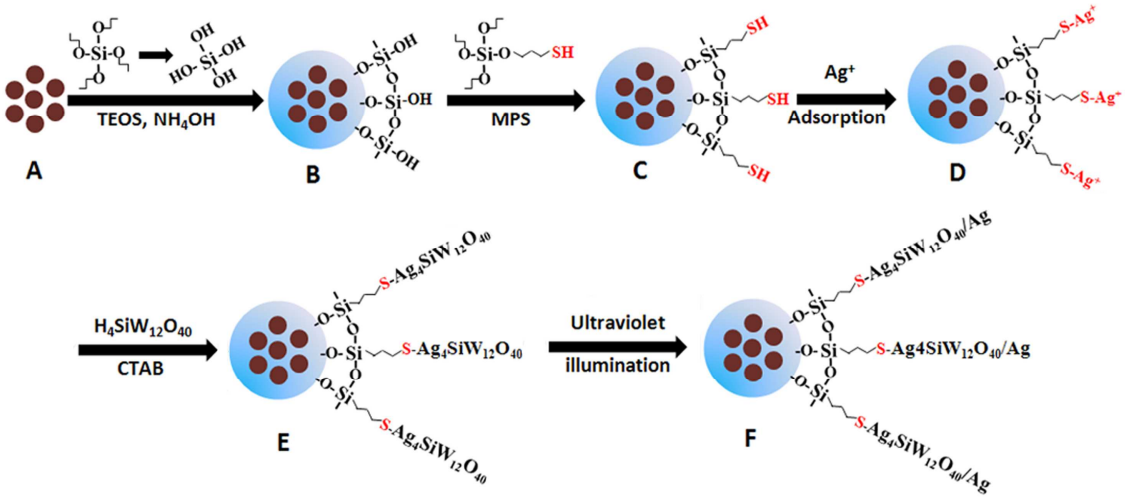

503

504 Figure 1

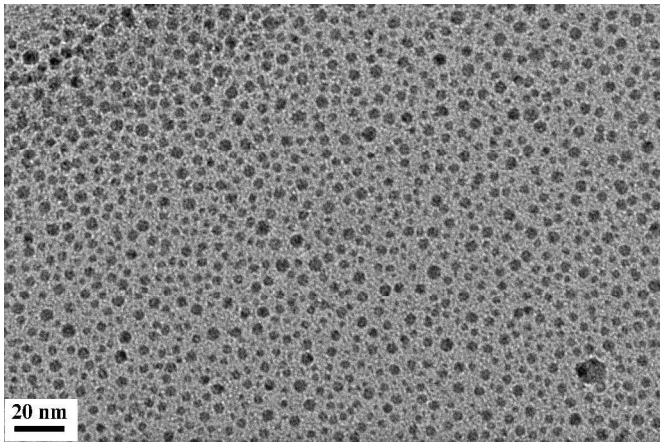

(a)

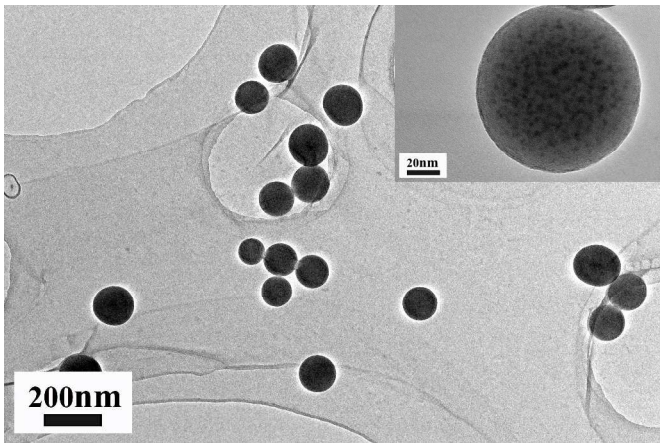

(b)

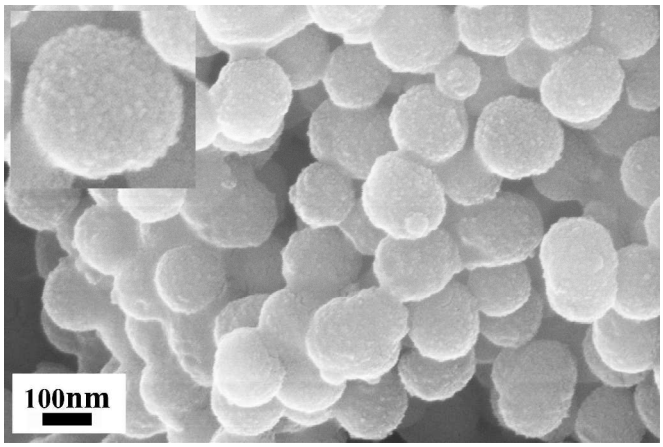

(c)

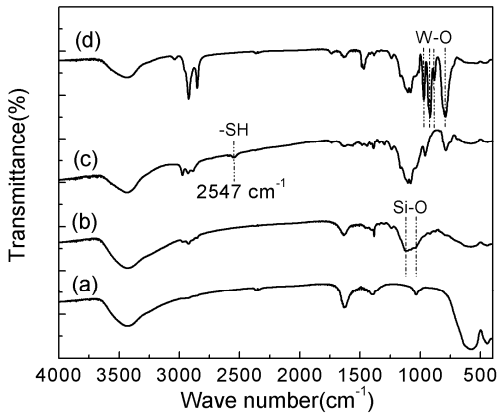

511

512 (d)

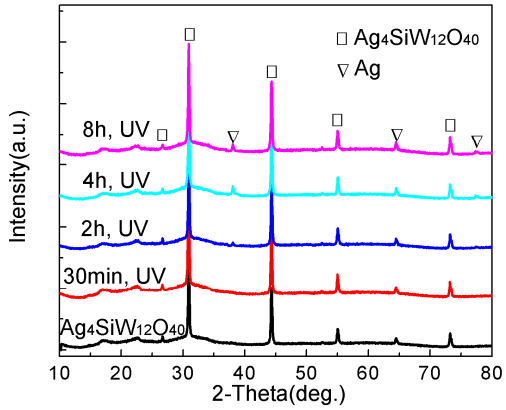

513

514 (e)

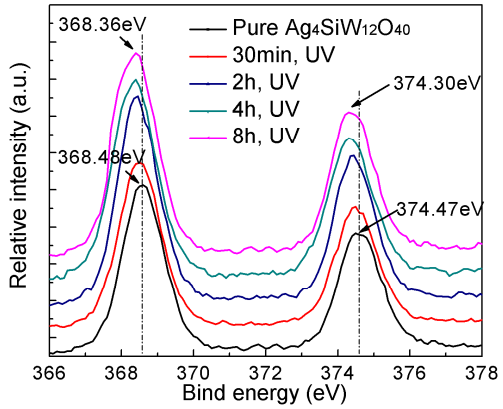

515

516 (f)

517 Figure 2

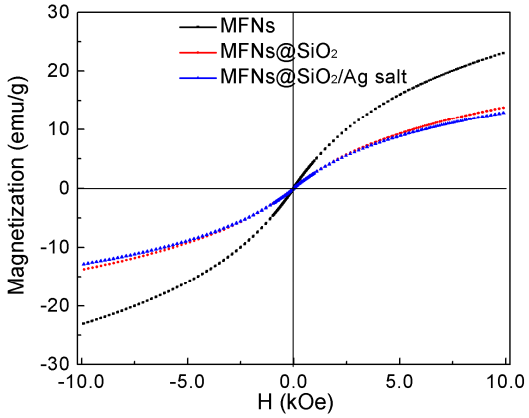

(a)

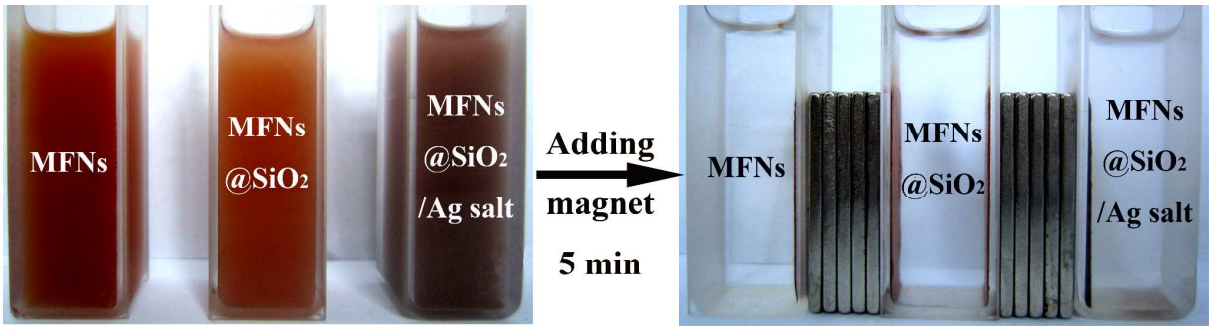

(b)

Figure 3

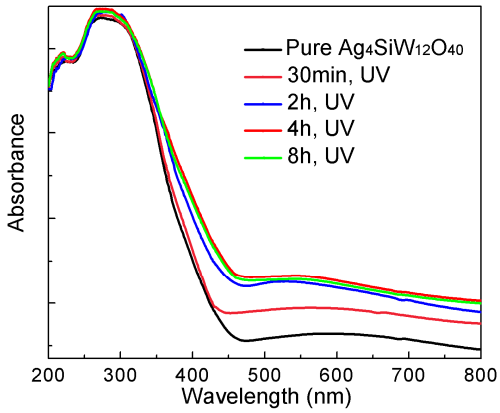

524

525 Figure 4

526

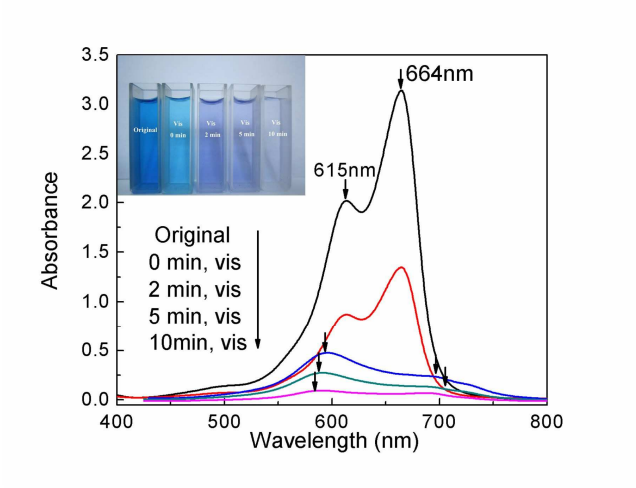

527

528 (a)

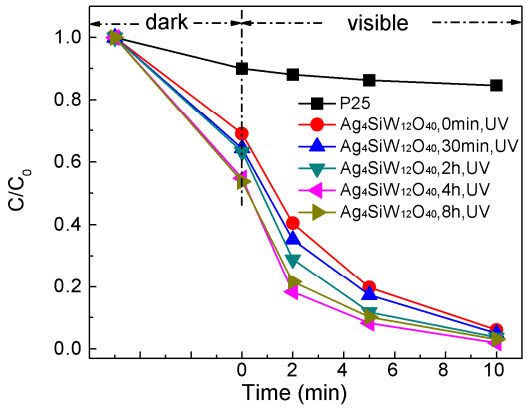

529

530 (b)

531 Figure 5

532

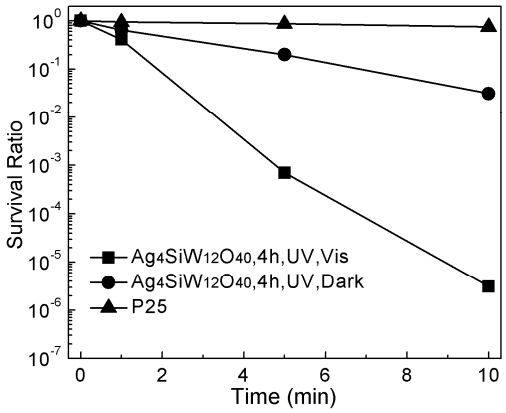

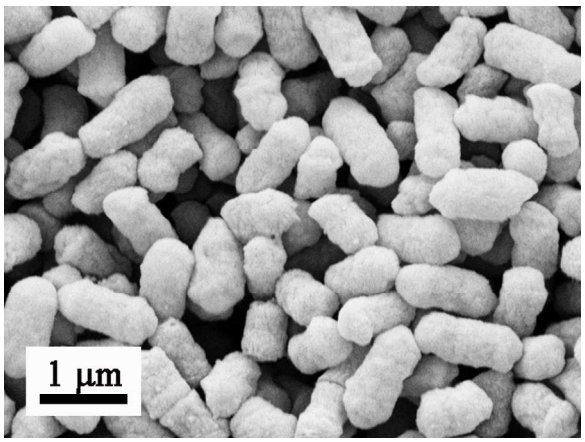

(a) (b)

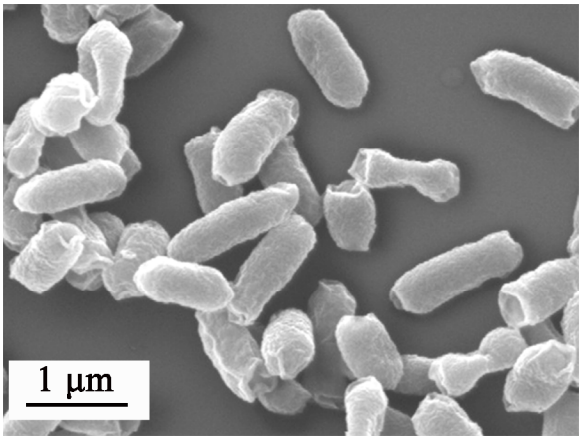

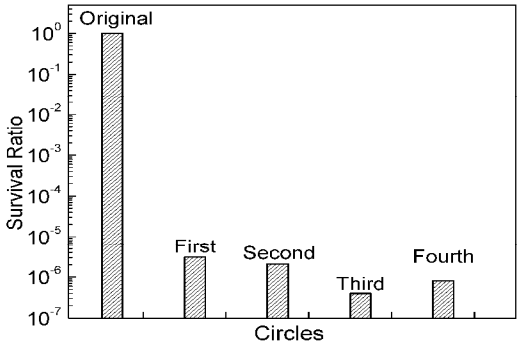

(c) (d)

Figure 6

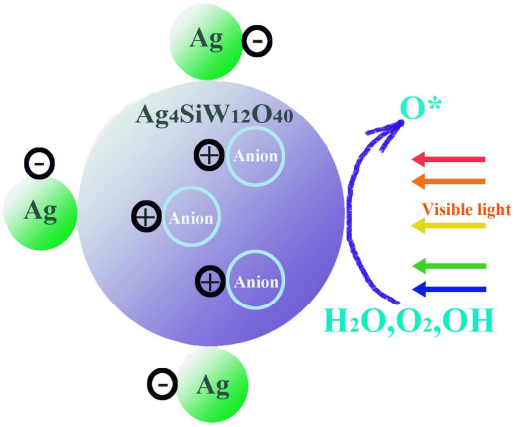

541

542 Figure 7